

Determination of impact parameter for CEE with digi-input neural networks

Botan Wang,^a Yi Wang,^{a,1} Dong Han,^a Zhigang Xiao^b and Yapeng Zhang^c

^a*Key Laboratory of Particle and Radiation Imaging, Department of Engineering Physics, Tsinghua University, Beijing 100084, China*

^b*Department of Physics, Tsinghua University, Beijing 100084, China*

^c*Institute of Modern Physics, Chinese Academy of Science, Lanzhou 730000, China*

E-mail: yiwang@mail.tsinghua.edu.cn

ABSTRACT: The impact parameter characterizes the centrality in nucleus-nucleus collision geometry. The determination of impact parameters in real experiments is usually based on the reconstructed tracks and hits, or the derived event-level observables. For the scheduled Cooler-storage-ring External-target Experiment (CEE), the low beam energy results in a reduction of dependency between the impact parameter and charged particle multiplicity, which decreases the validity of the explicit determination methods. This work implements a few neural networks that directly take the digitized signals from the external Time-of-flight detectors as input. The model with the best performance has shown a mean absolute error of 0.479 fm with the simulated U-U collisions at 0.5 AGeV. Performances of these models with digi inputs are compared with reference models with phase space inputs, showing the capacity of neural networks in handling the original but potentially interrelated digitized signal information.

KEYWORDS: Instrumentation and methods for time-of-flight (TOF) spectroscopy, Timing detectors, Resistive-plate chambers, Pattern recognition, cluster finding, calibration and fitting methods

ARXIV EPRINT: [2307.15355](https://arxiv.org/abs/2307.15355)

¹Corresponding author.

Contents

1	Introduction	1
2	Description of the task	3
3	Description of the Simulation	5
3.1	Dataset generation	5
3.2	Regression models	8
3.3	Test of the models	8
4	Performances and discussion	9
5	Conclusion	13
A	Structures and hyper-parameters of the models	13

1 Introduction

Relativistic nucleus-nucleus collision is one of the main approaches to studying the Equation of State (EoS) of the nuclear matter[1]. By designing the collision system and energy, the compressed matter is expected to reach a specific state in the Quantum Chromodynamics (QCD) phase diagram[2]. Although such a state evolution lasts only for tens of fm/c, results and evidence on physics issues such as critical point of phase transition[3], Quark-Gluon Plasma[4], color-superconductivity[5] can be made through the detection and analysis of the final-state particles. There are many colliders[6–8] or fixed-target facilities[9, 10] around the world whose detectors are built for the acceptance of collision products such as the charged particles, neutrons, gamma rays, and projectile fragments. The Cooler-storage-ring External-target Experiment (CEE)[11] is a fixed-target heavy-ion experiment that will run in an energy range of 0.5-1.2 AGeV. Time-of-flight (TOF) technique[12], which requires cooperation of tracking and timing detectors, is practiced for charged particle identifications. Figure 1 shows the detector layout of the CEE. Since there is a large variation of particle momentum with polar angles, two arrays of detectors are designed for identifying the particles at the front ($\theta < 25^\circ$) and large angle ($\theta > 25^\circ$). The Time Projection Chamber (TPC)[13] and the inner TOF (iTof)[14] system are installed inside the dipole magnet and cover the intermediate rapidity zone. As front-angle detectors, the Multi-Wire Drift Chamber (MWDC)[15] and the external TOF (eTOF)[16, 17] wall are placed downstream of the magnet for a longer distance. Figure 2 shows the phase space distribution, i.e. the particle distribution presented by the reduced rapidity y_0 and the reduced transverse momentum p_T/m , where the acceptances of the two detector arrays can be recognized. A T0 detector[18] is also included for start time measurements. A Zero-Degree Calorimeter (ZDC)[19] is placed at the most downstream, measuring the baryons for the reconstruction of event plane and centrality.

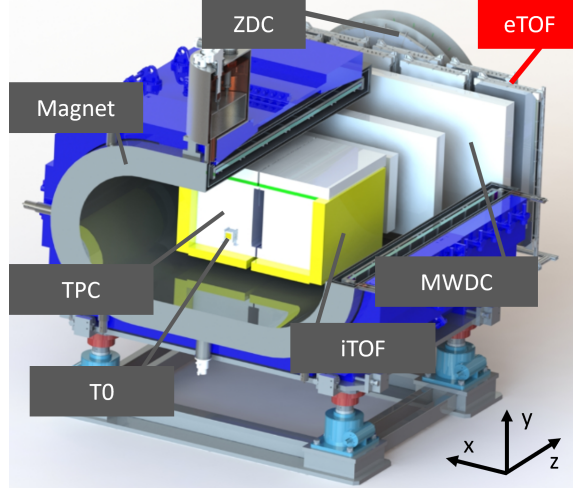


Figure 1. Detector layout of CEE.

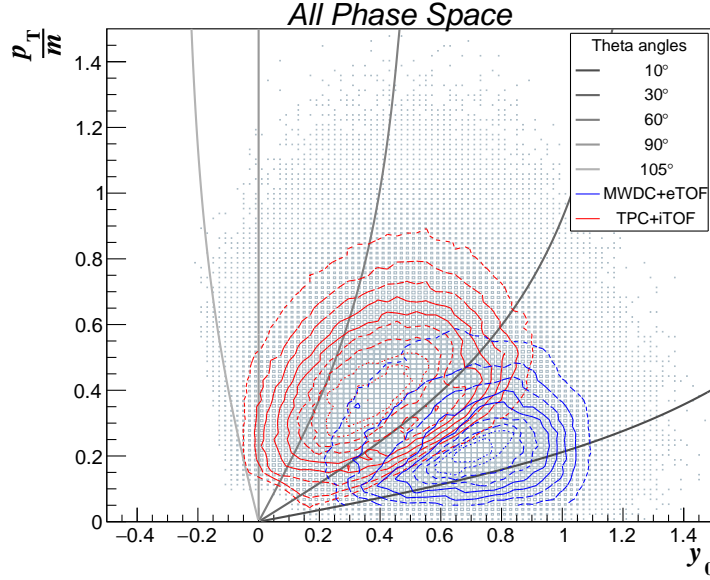


Figure 2. Phase space distribution of CEE. The size of the pixels stands for the particle density, and the contour shows the coverage of the forward and transverse detectors.

Given a fixed beam energy, the centrality serves as the most descriptive geometric quantity which determines the initial state of a collision. An equivalent description of centrality is the impact parameter b , which is defined as the perpendicular distance between the centers of both nuclei along the trajectory. More central collisions result in more interacting nucleons known as participants, and compressed nuclear matter with higher density. There are several EoS-related research topics, such as the collective and elliptical flow, and symmetry energy, which need the recognition of the central, semi-peripheral, and peripheral collisions[20, 21]. The most common method in experiments is to measure the distribution of a single observable with a strong correlation to the impact

parameter. Then the distribution can be processed by a sharp cut-off or Bayesian methods which give discrimination strategies[22–25]. Such observables include the total charged multiplicity, the transverse momentum, the number of intermediate-mass fragments, the total number of participant neutrons, etc. The fruitful collection of the above features also inspired the multivariate analysis, which turned the centrality determination into a typical instance of feature recognition. Since the 1990s, there have been works that apply Support Vector Machine (SVM)[26], Gradient Boosting Decision Tree (GBDT)[27], and several kinds of neural networks[28–30] to the regression of the impact parameters. Such works have two main characteristics: the regression or classification model should be trained with simulated data which can provide the target ‘TRUE’ impact parameter; the input variables to the models are the highly correlated observables obtained through event reconstruction.

The development of Artificial Intelligence and Deep Neural Networks (DNN) has expanded the capabilities of regression models in non-linear tasks and made it possible for models to handle data with primitive features. For recent works on centrality determination, tracks and hits of the final state particles, extracted from the detectors, have been considered as direct features. *F. Li, et al* translated the particle production into a phase space image in a 30×30 shape and implemented the Convolution Neural Network (CNN)[31] to regress the impact parameters[32]. Then they tested the precision of the method under the Au-Au collision data in an intermediate low beam energy range of 0.2-1.0 AGeV. *M. O. Kuttan, et al* were dedicated to developing a CNN-based model called PointNet which could handle the variable length and commutable input of hits and tracks[30]. The whole structure was applied to the regression of the impact parameter in Au-Au collisions at 10 AGeV.

The above works inspire the impact parameter determination of CEE. We propose the regression with DNNs using the channel response of the eTOF detectors as input. It is shown from the tests that the utilization of the detector data results in even higher prediction powers on the impact parameter than the common event-level features, such as phase space distribution. This paper is organized as follows: Section 2 describes the task of impact parameter determination in the context of CEE, basic information about the eTOF wall, and how the features from the eTOF detectors are extracted. Section 3 describes how the simulation is designed and carried out, including the data preparation and the DNN models. Section 4 shows the simulation results of the models. A summary is made in the last section.

2 Description of the task

The typical collision system for CEE is U-U at 0.5 AGeV. The collision energy is below the required threshold for most mesons and resonances, leaving the majority of the charged products as baryons like protons, deuterons, tritons and heavier ions[17]. As a result, the event fluctuation for central collisions is high, which deteriorates the centrality dependence with multiplicity. From the example of Au-Au collisions[30], we can read the precision from polynomial fit around 1 fm for events at 10 AGeV with $b = 1$ fm. However, such a prediction is not valid for events at 1 AGeV because the prediction stops around 2 fm. Given the expectation of high prediction uncertainty in the CEE condition, many strategies for centrality determination have been considered, for example, by using the angle distribution of energy deposition in ZDC, or by using reconstructed tracks of the full

system. It is expected that strategies based on different detectors as data sources can be combined into a powerful final predictor.

The eTOF wall is one of the ideal detector candidates for centrality determination thanks to the large coverage ($3.2 \times 1.6 \text{ m}^2$), high granularity (1344 channels in total), and fast signal shaping. The eTOF wall is composed of 24 Multigap Resistive Plate Chambers (MRPC) with 10 gas gaps of 0.25 mm thickness. Figure 3 shows the detector layout of the eTOF wall, where the MRPCs cover an active area of $3.2 \times 1.6 \text{ m}^2$. The eTOF wall contains 672 horizontal strips in total, read out from both ends. They are in the same size of $48 \times 1.5 \text{ cm}^2$ and arranged in an interval of 1.7 cm in every detector. The 6 smaller MRPCs in the inner region of the eTOF wall have 16 readout strips while the others have 32. The eTOF wall is divided into 7 columns which results in a **96×7 layout** of readout strips. The primitive signals, induced by the readout strips from the avalanches in MRPC's gas gaps, are amplified and discriminated by the NINO-based[33] Front-End Electronics (FEE)[34]. The outputting signals are recorded by the Time-to-Digital Module[34] for their leading and trailing time when the amplified signals cross a threshold (i.e. 150 mV for eTOF FEEs). The expected efficiency and time resolution of the eTOF MRPCs are better than 95% and 60 ps respectively, and have been verified on the real-size prototypes in the cosmic and beam tests.

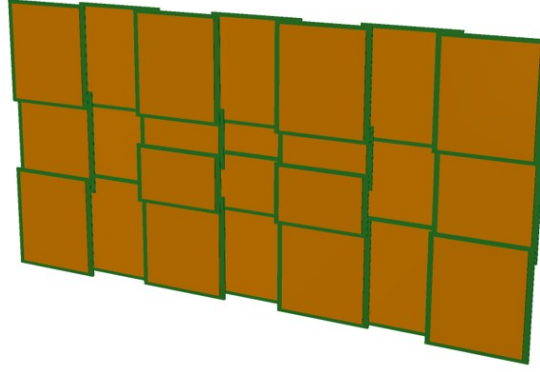


Figure 3. Detector layout of the eTOF wall.

Because of the low collision energy and the limited front-angle coverage, the monotonicity between the accepted particle multiplicity and impact parameter loses totally for the eTOF wall, as shown in Figure 4. The multiplicity starts to drop when the impact parameter goes under 5 fm, likely due to the increase of average transverse momentum in central collisions. Therefore, it is important to consider multiple features when using eTOF as the data source. In other words, not only the accepted hit multiplicity, but also their temporal and spatial features should be included. Such features can be easily extracted from the digitized signals, i.e. the recorded leading and trailing time mentioned above. The average time of both ends of the strip represents the hit time, and the differential time represents the hit position along the strip. The channel layout of the eTOF wall can be considered as a gridding of the phase space. Therefore, it is reasonable to believe that the digi-input strategy will not lose either the information or the granularity in the context of centrality determination.

This work gives a simulation study using the simulated collisions and the resulting digitized

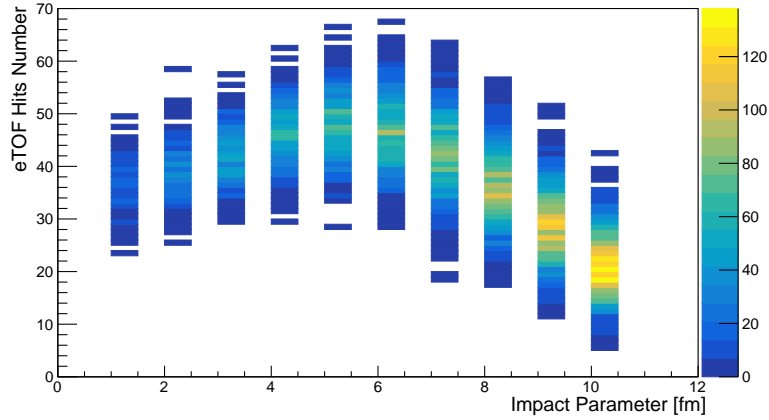


Figure 4. Multiplicity distribution of eTOF with respect to impact parameters.

signals from eTOF. However, it is important to maintain the validity of the methods and models when using the experimental signals in future practices. At least two factors should be concerned on the quality of the experimental data. The first is the correct event assembly, which requires that the acquired signals are from a single collision. In CEE condition, over 98% of the in-event charged particles reach the TOF detectors within a time window of 25 ns. Accordingly, the time windows for triggering and data acquisition are 75 ns and 1 μ s respectively. Given the interaction rate of 10 kHz, the channel response of eTOF in the same event can be organized correctly. The second factor is the stability of the data distribution, such as the reconstructed time and position. It will introduce prediction errors to the model if the experimental data distribution is biased or unstatic. During the operation of CEE, parameters from both the detectors (signal propagation speed, time resolution, etc.) and the electronics (processing time of readout, triggering, etc.) are stable with time. Given a feature distribution independent with instrument conditions, proper normalization can be carried out to minimize the divergence between the simulation and experimental data distributions.

3 Description of the Simulation

3.1 Dataset generation

Datasets in this paper are generated following the procedures below: Firstly, collision data is generated which gives the produced steady particles and their initial kinetic attributes. The physics model of the collision is Isospin-dependent Quantum Molecular Dynamics (IQMD)[35], and the coalescence of nucleons is processed after the IQMD calculation since ion yield is significant in the CEE energy. Then, CeeRoot[36], a platform based on the FairRoot[37] framework, carries out the simulation which organizes the collision data together with detector geometry and the Geant4 transport model. Finally, with proper pre-processing, we obtain the dataset for model training and testing.

During the CeeRoot simulation, the digitization method[38], which translates the Monte-Carlo points of eTOF into the digitized signals, is carefully designed according to the experimental conditions. Processes of detector response such as noise hit, hit cluster size, time resolution, and

time delay, have been considered in the digitization. Noise hits are added randomly following the typical MRPC noise level of 1 Hz/cm². The hit times for noise strips are obtained by sampling the uniform distribution U(0, 100) ns where 100 ns is the typical time window for event assembly. The hit positions for noise strips are sampled from U(-1.5, 1.5) ns which corresponds to the range of strip length. Due to the transverse diffusion of the avalanche charge, hits with multiple strips firing should be considered in the simulation. In digitization, such an effect is simulated by sampling a cluster size distribution measured in detector tests. For each digitized signal, the signal leading time T_{leading} is calculated as follows:

$$T_{\text{leading}} = t_{\text{hit}} + \frac{|x_{\text{end}} - x_{\text{hit}}|}{v_{\text{prop}}} + \Delta t_{\text{ele}} + \Delta t_{\text{reso}} \quad (3.1)$$

where t_{hit} , x_{hit} are the hit time and position, x_{end} is the position of the strip end, v_{prop} is the signal propagation speed along the strip. Δt_{ele} is the time delay of the electronics, which is sampled from uniform distribution [0, 5) ns and constant for each specific channel. Δt_{reso} is sampled from Gaussian distribution with 100 ps standard deviation, representing the time resolution. It is inferred from the data normalization that the time delay effect can be eliminated in the model regression and prediction, which is very helpful because of the complexity of the measurement of channel time delay. As the time-slewing effect has not been implemented in the digitization method, the 100 ps smearing is chosen according to the measurement before the time-slewing correction in the cosmic tests[38].

We simulated 1.21 million events of U-U collisions at 0.5 AGeV. The events are distributed uniformly from impact parameter $b=0.0$ fm to $b=12.0$ fm with 0.1 fm step. The total events are randomly split into the train and test set with an 8:2 ratio. Two datasets are generated based on the test set: one is the so-called *bdb* test set with 120k events, and the other is the uniform test set with all the 242k events. The *bdb* test set is generated following the collision geometry where the differential cross section is proportional to the impact parameter: $d\sigma \propto bdb$. It is used for evaluating the overall performance of the models because it is close to the realistic collisions; the uniform test set is for the assessment of performance in the function of the impact parameters. The train set has 968k events in which 80% are used for model fitting and 20% are used for early-stop decision (see Section 3.3) after each training epoch.

For each simulated event, we collect the features from the total 672 readout strips, including the **hit flag, hit time, and hit position**. The hit flag is set to 1 if there are signals generated from both ends of the strip. The hit time is calculated as the average time of both ends and the hit position is the half difference of the both-end time values. Such calculation, despite its simplicity, provides features with clearer physics meaning. For strips with no hit detected, the hit flag is set to zero and the time and position are set to the local average value from the training dataset. The choice of data imputation here is made in order to obtain zero values after the normalization of the time and position features. The purpose of keeping zero values for the non-fired nodes is to implicitly stop the forward propagation of their features. The first dense layer is designed to exclude the intercept term, so that the non-fired nodes with zero input values always result in zero outputs. The absence of trainable intercept have no effect on the capability of the dense layer because the weight on the hit flag plays an equivalent role. Moreover, the zero-value nodes have no function in the attention layer when the linear combination of the nodes are calculated with their attributes. Figure 5 shows

the counting rate distribution of the 672 readout strips for the eTOF wall. A descending counting rate is shown due to the collision in fix-target mode.

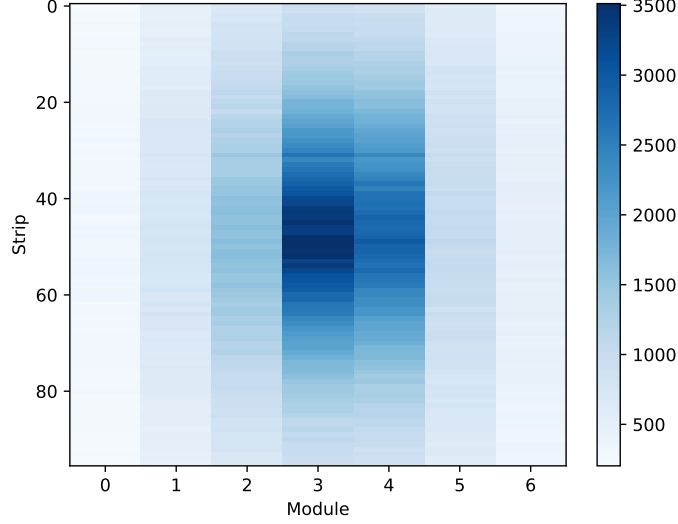


Figure 5. Counting rate distribution of 672 readout strips for eTOF wall. The color bar is in Hz.

To compare the model performance with other work, we generate the **phase space dataset with 30x30 binning**. The range of the phase space used for binning is defined as $y_0 \in [-0.5, 1.5]$, $p_T/m \in [0, 1.5]$. Figure 6(a) shows the cumulative images of the phase space with impact parameters, where the evolution of the image shape can be easily recognized. However, for a single event, features get more indistinct due to the event fluctuation, as demonstrated in Figure 6(b). Two sets of phase space data, with acceptances covered by CEE and only eTOF, have been prepared for a comparison study.

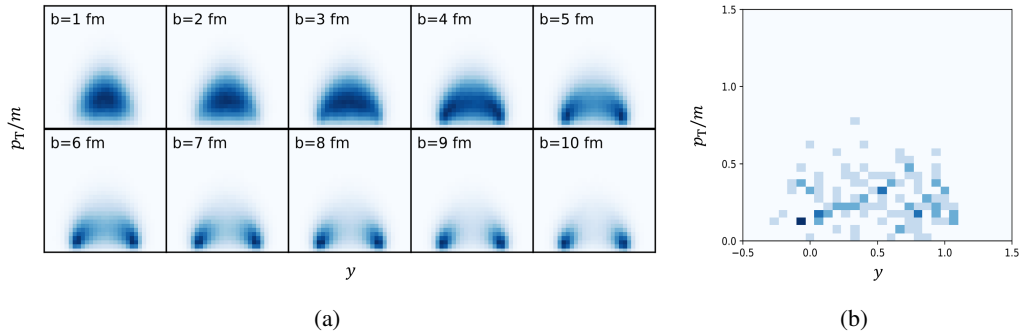


Figure 6. (a) The resampling phase space images in the acceptance of CEE with different impact parameters. Each image is filled with 10k events with the impact parameter shown in the legend. The binning of the image is 30x30. (b) Image of an event with $b = 6$ fm.

3.2 Regression models

Two DNN models have been implemented for the task: CNN and Graph Attention network (GAT)[39, 40]. The structures of the two models are demonstrated in the Appendix Figure 12 and 13. For both models, a dense layer is implemented at the entrance of the input data to encode the three features for each readout strip. The encoder outputs 762×64 hidden features for further extractions with two sequential CNN or GAT layers. Finally, all the output features are flattened and decoded to the impact parameter prediction by a dense layer.

CNN extracts the correlation between geometrically local features and trainable kernels through convolution, and it is one of the most popular algorithms in image recognition. For this work, the phase space distribution can be treated as an image and is capable of inputs with multi-features, which is similar to the RGB channels of the image. Besides the phase space input, CNN is also capable of processing digitized signal input. In this mode features from the 762 strips are arranged into a $96 \times 7 \times 3$ shape to reflect the geometry layout. The convolutional kernel in CNN is a key module for feature extraction, and its size should be modified according to the geometry coverage that the input data includes. The kernel size of the first convolutional layer is set to 5×5 for phase space input, while for digi input it is 3×32 because of the strip dimension. The other hyper-parameters of the models can be found in the Appendix Table 2.

Graph Neural Networks (GNN) have recently risen as a popular machine learning model with the capability of graphic structure handling. For nuclear collisions, data of the produced tracks, hits, or even signals can be regarded as graph data, in which each individual, or node in the concept of a graph, is potentially connected with others under the collision dynamics. GAT is one of the GNNs that provides robustness in dynamic graphs. It trains a universal and trainable agent for calculating the attention weights between any pair of nodes. Then the node features can be transferred as a combination of itself and its neighbouring nodes according to the attention weights. Equation 3.2 and 3.3 describes the principle of the GAT layer¹. Firstly, the attention weights α_{ij} are calculated, where \vec{h}_i stands for the input features of node i , σ the activation function, W and \vec{a} the trainable weight matrix and vector. Then, the output features \vec{h}'_i is obtained as the attention weighted combination of the encoded input features from the self and neighboring nodes \mathcal{N}_i .

$$\alpha_{ij} = \frac{\exp\left(\vec{a}^T \sigma\left(\left[W\vec{h}_i || W\vec{h}_j\right]\right)\right)}{\sum_{k \in \mathcal{N}_i} \exp\left(\vec{a}^T \sigma\left(\left[W\vec{h}_i || W\vec{h}_k\right]\right)\right)} \quad (3.2)$$

$$\vec{h}'_i = \sum_{j \in \mathcal{N}_i} \alpha_{ij} W \vec{h}_j \quad (3.3)$$

3.3 Test of the models

The tests in this paper, along with the key settings, are listed in Table 1. They are designed for different purposes of performance evaluation and validation. Firstly, to evaluate the model performances, CNN, GAT, and fully connected (FC) neural networks are implemented to regress the hit data of eTOF. Secondly, to compare the data inputs, CNN models are trained with phase space data and digitized signal data at the forward angle respectively. Finally, for the discussion

¹In this work, GATv2 structure[40] is implemented for better reported performance over GAT.

of further expansion of acceptance with large angle detectors included, we conduct a comparative study with the CNN model to regress the phase space data of the forward angle and total acceptance of CEE.

In this work, the graph in GAT network is constructed by connecting every two readout strips, which leaves the network to learn the edge attributes. GAT has a masked attention feature which allows eliminating attention weights of some predefined edges. Based on the characteristics, we tested the performances of GAT networks when, for each node, the ones outside the kernel of the CNN (3×32) and the ones within the kernel are masked respectively. The tests, labeled as GAT-HIT-FW-f and GAT-HIT-FW-c, can provide evidences on which nodes, farther or closer, are more important to a specific node.

For all the models, mean square error is used in the training as the loss function. An early-stop strategy is implemented for keeping the best weights of the DNNs when the performance in the valid data is not improved for 10 epochs. The best weights were reached after 10-40 epochs of training, depending on the models. Overfitting is not visible in this work since the data amounts are large enough to represent the overall feature distribution. Moreover, the tests have been evaluated on their stability with different train-test data splits.

Table 1. The test settings and regression performances in this work.

Test label	Acceptance	Type of data input	Network	MAE [fm]	MSE [fm ²]	R^2
CNN-PS-FW	Forward	Phase space	CNN	0.583	0.585	0.927
CNN-PS-TOT	Overall	Phase space	CNN	0.269	0.108	0.987
CNN-HIT-FW	Forward	Hit	CNN	0.506	0.435	0.946
GAT-HIT-FW	Forward	Hit	GAT	0.479	0.394	0.951
GAT-HIT-FW-f	Forward	Hit	GAT	0.487	0.405	0.951
GAT-HIT-FW-c	Forward	Hit	GAT	0.492	0.411	0.949
FC-HIT-FW	Forward	Hit	FC	0.547	0.536	0.934

4 Performances and discussion

The performance of the tests is evaluated by the following indicators: Mean Absolute Error (MAE), Mean Square Error (MSE) and goodness of fit R^2 . MAE and MSE are calculated with Equation 4.1 and 4.2 respectively:

$$\sigma_{\text{MAE}} = \frac{1}{n} \sum_n |b_{\text{pred}} - b_{\text{true}}| \quad (4.1)$$

$$\sigma_{\text{MSE}} = \frac{1}{n} \sum_n (b_{\text{pred}} - b_{\text{true}})^2 \quad (4.2)$$

The R^2 is defined as follows:

$$R^2 = 1 - \frac{\sum_n (b_{\text{pred}} - b_{\text{true}})^2}{\sum_n (b_{\text{pred}} - \bar{b})^2} \quad (4.3)$$

where n is the size of the data for validation or test, and \bar{b} stands for the average value of the impact parameters.

Table 1 lists the performances of the tests under the bdb test set. It is reasonable to find that the CNN-PS-TOT model has the best performance for the input features from the total phase space. It can be treated as an estimation of the determination capability in the condition of the CEE spectrometer and energy. The performance of CNN-PS-FW shows the capability with phase space identified by the forward detectors, and it also serves as a reference model for comparison with others that take the forward TOF data as input. It is inspiring to find that the models with eTOF hit input show superior performances than the reference model, with decreases of the MAE by 6-18%. Such an improvement in the HIT-FW tests indicates that the digitized signal data, despite the ambiguity, preserves implicit patterns that can be extracted by DNN models in diverse forms. For example, the position information can potentially increase the equivalent granularity of the HIT-FW models, and the time may reveal the secondary particle types. Yet, these features are no longer reserved in the phase space inputs.

Among the HIT-FW tests, the GAT model has the highest precision in centrality prediction. The dependency of the prediction resolution (MAE) and impact parameters for the HIT-FW tests is investigated, as shown in Figure 7. Each data point is defined on the uniform test set with an impact parameter interval of $[-0.25, 0.25]$ fm. For example, the first point corresponds to the data in $[0, 0.5)$ fm. The three models show some similar patterns in their curves but for most centrality including the central region, the GAT model outperforms other models significantly given the uncertainty of 0.4% (50k events for each data point).

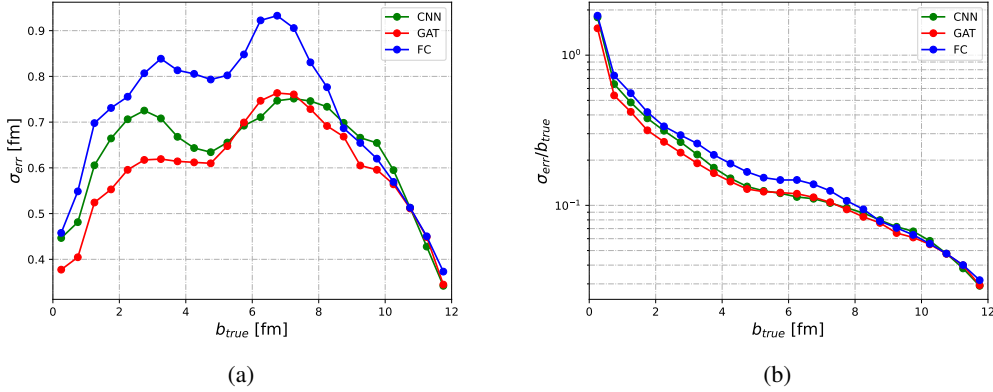


Figure 7. (a) MAE deviations of digi-input models with respect to impact parameters. (b) Relative MAE deviations in the function of impact parameters.

The aggregation mechanism of neighbors in the GAT structure contributes to the overall superiority because it helps eliminate the randomness of the single hits. Such a principle is also embodied in the CNN model which is based on spatial convolution. However, the size of the convolution kernel confines the range of the aggregation locally. It can be seen that masking either the local (GAT-HIT-FW-f) or the distant nodes (GAT-HIT-FW-c) from transferring their features will decrease the prediction power of the GAT model.

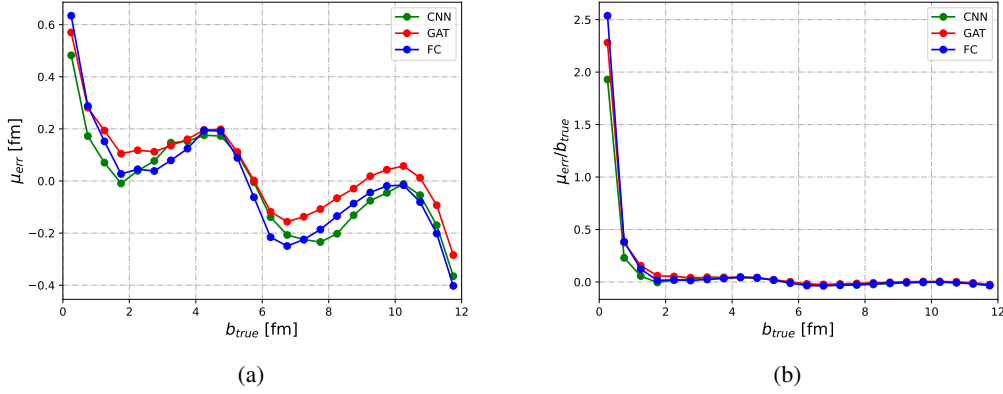


Figure 8. (a) Biases of digi-input models with respect to impact parameters. (b) Relative biases of digi-input models with respect to impact parameters.

Figure 8 shows the relative prediction biases of the HIT-FW tests with centrality. The three models show satisfying bias suppression. For very central collisions ($b < 1.5$ fm), the relative bias rises significantly, likely due to the high prediction uncertainty in this centrality region. The least accuracy of the GAT model will not have significant influence on its application, given the best resolution which includes the bias.

The prediction of the GAT model on the bdb test dataset is examined visually in Figure 9. A good correlation is shown which agrees with the results in Table 1. It seems that the linear relationship is interfered at around 6 fm, where the prediction error is higher than other ranges in Figure 7. Similar patterns are visible for other models as well. Figure 10 shows the dependency of impact parameters to the correlated collision features. $b_{CNN-TOT}$, b_{CNN-FW} , b_{GAT} represent the predicted impact parameters from model CNN-PS-TOT, CNN-PS-FW and GAT-HIT-FW respectively, M_{tot} the multiplicity of total acceptance, $p_{T,tot}$ the summation of reduced transverse momentum for charged particles in the overall acceptance, M_{fw} , $p_{T,fw}$ the ones in the forward acceptance. It is shown that the correlation of the features at forward acceptance is weak for impact parameters around 6 fm. It may explain the low precision of such a region for forward predictors. When the impact parameter decreases, the secondary particle distribution moves toward the mid-rapidity region which goes beyond the coverage of eTOF. Consequently, the forward quantities lose the monotonicity and decline, which supports why the model fed with overall phase spaces shows the best performance. In general, the models trained from either the phase spaces or the digitized signals succeed in reproducing the dependencies between the impact parameter and the collision quantities as simulation shows.

A significant characteristic of the GAT model is the interpretability of graphical relations. We investigate the importance of the attention weights among the 672 readout strips with the help of NetworkX[41], a tool for visualizing and analysing the graph. Figure 11 shows the graph visualization of the GAT model in predicting the test dataset. The grey cloud is composed of an intense crowd of black edges whose widths stand for the average value of the attention weights. The nodes in the graph are arranged following the Fruchterman-Reingold force-directed algorithm[42],

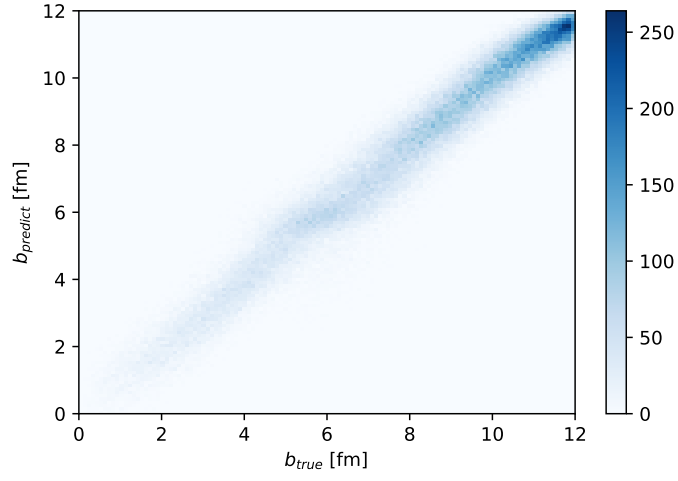


Figure 9. Distribution between the predicted impact parameters by GAT-HIT-FW and the true impact parameters.

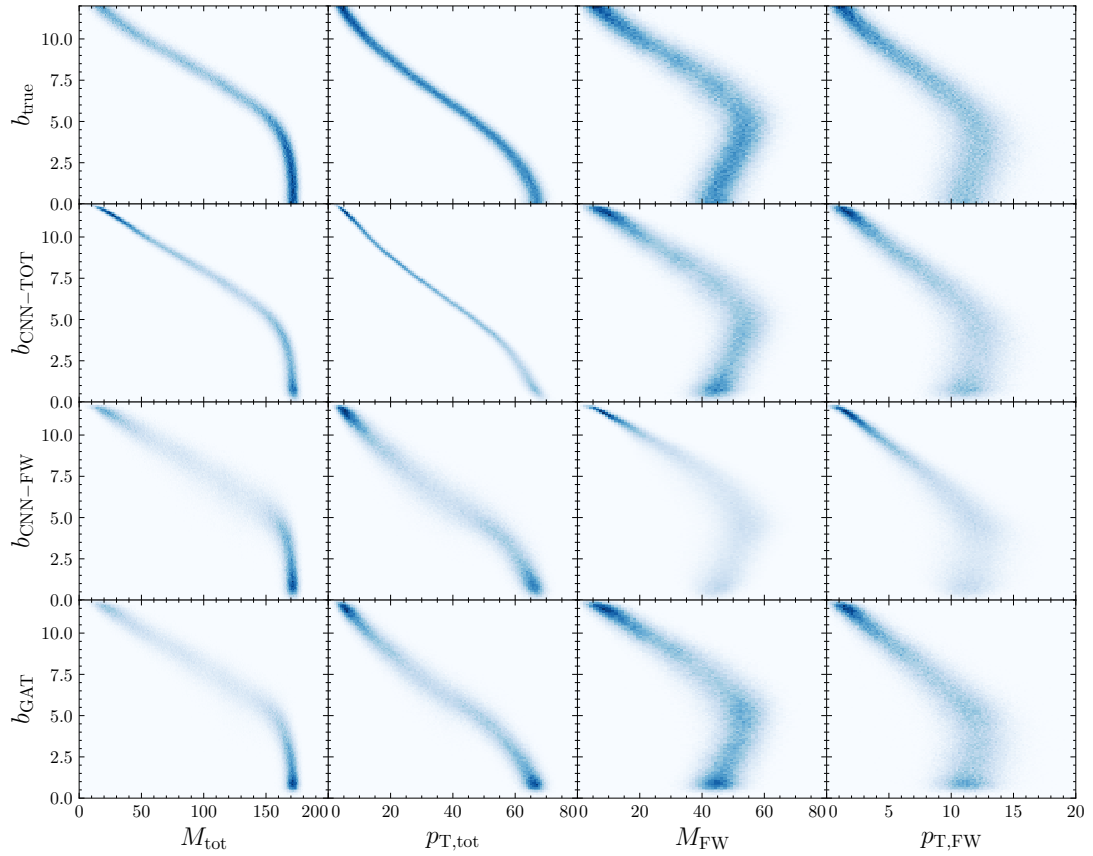


Figure 10. Dependency of the true and predicted impact parameters to the correlated collision features.

and as a result, nodes with stronger connections to others will be dragged to the central area. The nodes in the graph are colored according to the total signal counts on the strip. It is observed that the light-colored nodes, which represent the strips from the inner area of eTOF, have a higher importance in the contribution of the features, which indicates that the features from these strips can be effectively transmitted to the other strips, even for those at the outer region.

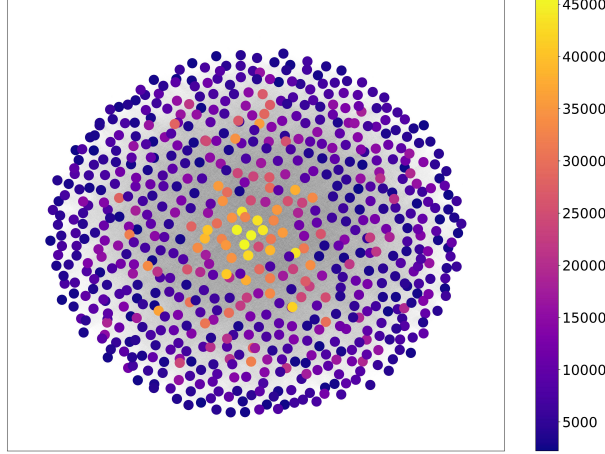


Figure 11. Visualization of the edge weights between 672 readout strips after training.

5 Conclusion

This work is one of the efforts on the determination of impact parameters for CEE. DNN-based models are regarded as appropriate approaches as high dimensional features are needed in low collision energies. We propose that the original digitized signals from the eTOF MRPCs are informative as input, and the DNN models are powerful enough to extract the predictive features. Several structures of DNN models are implemented and tested, showing that the prediction precision with digitized signal inputs exceeds the phase space inputs of the same acceptance by up to 18%. Among the models in our tests, the GAT model reaches the best prediction precision of 0.479 fm in mean absolute error, and the prediction power outperforms other models significantly for central collisions. It is also examined that larger acceptance will result in better performance, which encourages further investigations of including the channel responses from other subsystems.

A Structures and hyper-parameters of the models

Acknowledgments

This work is supported by the National Natural Science Foundation of China under Grant No. 11927901, 11420101004, 11735009, U1832118, and by the Ministry of Science and Technology

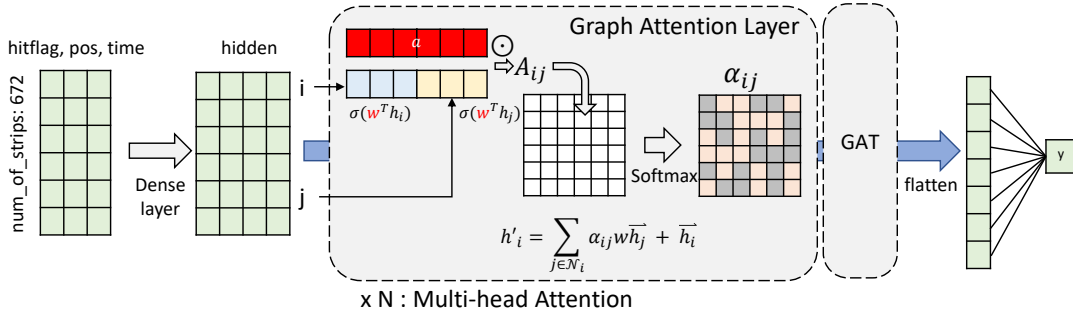


Figure 12. Structure of the GAT network used in this work.

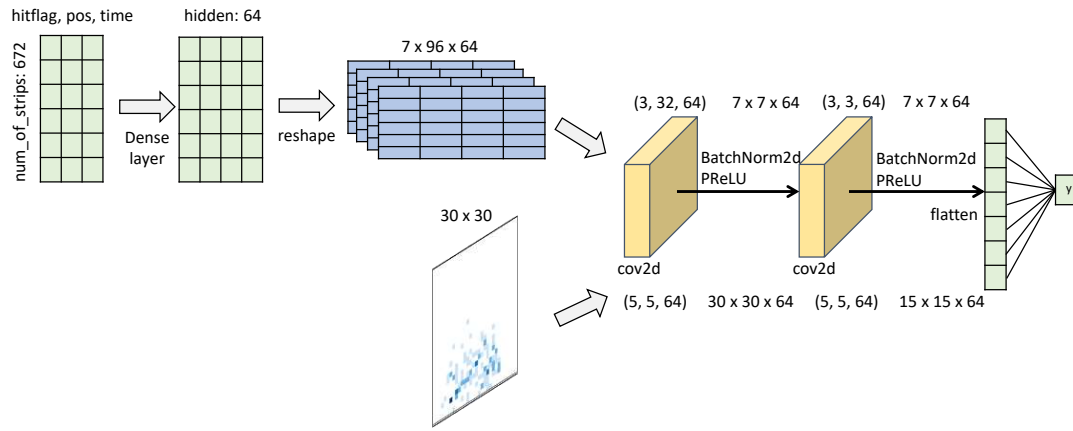


Figure 13. Structure of the CNN network used in this work. The upper flow processes digitized signal inputs while the lower flow processes phase space inputs.

Table 2. Hyperparameters for the models in this work.

	GAT		FC
Hidden size	64 into 4 heads	Hidden size	64
Num. layers	2	Num. layers	2
Learning rate	5x10-4	Learning rate	5x10-4
Learning rate strategy	Warmup and exponential decay	Learning rate strategy	Exponential decay
	CNN-HIT		CNN-PS
Hidden channels	64	Hidden channels	64
Num. conv. layers	2	Num. conv. layers	2
Kernel size 1	(3, 32, 64)	Kernel size 1	(5, 5, 64)
Kernel size 2	(3, 3, 64)	Kernel size 2	(5, 5, 64)
Learning rate	5x10-4	Learning rate	5x10-4
Learning rate strategy	Exponential decay	Learning rate strategy	Exponential decay

under Grant No. 2018YFE0205200, 2016YFA0400100.

References

- [1] M. Jacob and J. Tran Thanh Van. Quark matter formation and heavy ion collisions: A general review and status report. *Phys. Rep.*, 88(5):321–413, August 1982.
- [2] Sourendu Gupta et al. Scale for the Phase Diagram of Quantum Chromodynamics. *Sci*, 332(6037):1525–1528, June 2011.
- [3] Xiaofeng Luo and Nu Xu. Search for the QCD critical point with fluctuations of conserved quantities in relativistic heavy-ion collisions at RHIC: an overview. *Nucl. Sci. Tech.*, 28(8):112, July 2017.
- [4] Barbara V. Jacak and Berndt Müller. The Exploration of Hot Nuclear Matter. *Sci*, 337(6092):310–314, July 2012. Publisher: American Association for the Advancement of Science.
- [5] Mark G. Alford et al. Color superconductivity in dense quark matter. *Rev. Mod. Phys.*, 80(4):1455–1515, November 2008.
- [6] K.H. Ackermann et al. STAR detector overview. *Nucl. Instrum. Methods Phys. Res. A*, 499(2-3):624–632, March 2003.
- [7] The ALICE Collaboration et al. The ALICE experiment at the CERN LHC. *J. Inst.*, 3(08):S08002, aug 2008.
- [8] Yongsun Kim. The Detector Development and Physics Program in sPHENIX Experiment at RHIC. *Nucl. Phys. A*, 982:955–958, February 2019.
- [9] Kathryn C. Meehan. Fixed Target Collisions at STAR. *Nucl. Phys. A*, 956:878–881, December 2016.
- [10] Tetyana Galatyuk. HADES overview. *Nucl. Phys. A*, 931:41–51, November 2014.
- [11] LiMing Lü et al. Conceptual design of the HIRFL-CSR external-target experiment. *Sci. China Phys., Mech. Astron.*, 60(1):012021, January 2017.
- [12] Yi Wang and Yancheng Yu. Multigap Resistive Plate Chambers for Time of Flight Applications. *Appl. Sci.*, 11(1):111, December 2020.
- [13] Wen Huang et al. Laser test of the prototype of CEE time projection chamber. *Nucl. Sci. Tech.*, 29(3):41, March 2018.
- [14] X. Wang et al. CEE inner TOF prototype design and preliminary test results. *J. Instrum.*, 17(09):P09023, September 2022. Publisher: IOP Publishing.
- [15] Han Yi et al. Prototype studies on the forward MWDC tracking array of the external target experiment at HIRFL-CSR. *Chin. Phys. C*, 38(12):126002, December 2014.
- [16] B. Wang et al. The CEE-eTOF wall constructed with new sealed MRPC. *J. Instrum.*, 15(08):C08022–C08022, August 2020. Publisher: IOP Publishing.
- [17] Botan Wang et al. The external time-of-flight wall for CEE experiment. *Eur. Phys. J. C*, 83(9):817, September 2023.
- [18] Dongdong Hu et al. Extensive beam test study of prototype MRPCs for the T0 detector at the CSR external-target experiment. *Eur. Phys. J. C*, 80(3):282, March 2020.
- [19] Li-Ke Liu, Hua Pei, Ya-Ping Wang, Biao Zhang, Nu Xu, and Shu-Su Shi. Event plane determination from the zero degree calorimeter at the cooling storage ring external-target experiment. *NUCL SCI TECH*, 34(7):100, July 2023.

- [20] Supriya Goyal. Impact parameter dependence of collective flow and its disappearance for different mass asymmetries. *Eur. Phys. J. A*, 49(12):153, December 2013.
- [21] Varinderjit Kaur et al. On the elliptical flow and mass asymmetry of the colliding nuclei. *Phys. Lett. B*, 697(5):512–516, March 2011.
- [22] C. Cavata et al. Determination of the impact parameter in relativistic nucleus-nucleus collisions. *Phys. Rev. C*, 42(4):1760–1763, October 1990.
- [23] Michael L. Miller et al. Glauber Modeling in High-Energy Nuclear Collisions. *Annu. Rev. Nucl. Part. S.*, 57(1):205–243, 2007. _eprint: <https://doi.org/10.1146/annurev.nucl.57.090506.123020>.
- [24] J. D. Frankland et al. Model independent reconstruction of impact parameter distributions for intermediate energy heavy ion collisions. *Phys. Rev. C*, 104(3):034609, September 2021.
- [25] Sruthy Jyothi Das et al. Relating centrality to impact parameter in nucleus-nucleus collisions. *Phys. Rev. C*, 97(1):014905, January 2018.
- [26] J De Sanctis et al. Classification of the impact parameter in nucleus–nucleus collisions by a support vector machine method. *J. Phys. G: Nucl. Part. Phys.*, 36(1):015101, January 2009.
- [27] Fupeng Li et al. Application of artificial intelligence in the determination of impact parameter in heavy-ion collisions at intermediate energies. *J. Phys. G: Nucl. Part. Phys.*, 47(11):115104, November 2020.
- [28] F. Haddad et al. Impact parameter determination in experimental analysis using a neural network. *Phys. Rev. C*, 55(3):1371–1375, March 1997.
- [29] Christophe David, Marc Freslier, and Jörg Aichelin. Impact parameter determination for heavy-ion collisions by use of a neural network. *Phys. Rev. C*, 51(3):1453–1459, March 1995.
- [30] Manjunath Omana Kuttan et al. A fast centrality-meter for heavy-ion collisions at the CBM experiment. *Phys. Lett. B*, 811:135872, December 2020.
- [31] Alex Krizhevsky, Ilya Sutskever, and Geoffrey E. Hinton. ImageNet classification with deep convolutional neural networks. *Commun. ACM*, 60(6):84–90, May 2017.
- [32] Fupeng Li et al. Application of machine learning in the determination of impact parameter in the Sn 132 + Sn 124 system. *Phys. Rev. C*, 104(3):034608, September 2021.
- [33] F. Anghinolfi et al. NINO: an ultra-fast and low-power front-end amplifier/discriminator ASIC designed for the multigap resistive plate chamber. *Nucl. Instrum. Meth A*, 533(1-2):183–187, November 2004.
- [34] Jiaming Lu et al. Readout Electronics Prototype of TOF Detectors in CEE of HIRFL. *IEEE Trans. Nucl. Sci.*, 68(8):1976–1983, August 2021.
- [35] C. Hartnack et al. Modelling the many-body dynamics of heavy ion collisions: Present status and future perspective. *Eur. Phys. J. - Hadrons Nucl.*, 1(2):151–169, February 1998.
- [36] CeeRoot: CEERoot simulation and analysis package.
- [37] M Al-Turany et al. The FairRoot framework. *J. Phys.: Conf. Ser.*, 396(2):022001, December 2012.
- [38] B. Wang et al. A simulation and analysis framework for CEE-eTOF. *J. Inst.*, 17(07):P07024, July 2022.
- [39] Petar Velic̃kovic et al. GRAPH ATTENTION NETWORKS. page 12, 2018.
- [40] Shaked Brody, Uri Alon, and Eran Yahav. How attentive are graph attention networks?, 2022.

- [41] NetworkX — NetworkX documentation.
- [42] Thomas M. J. Fruchterman and Edward M. Reingold. Graph drawing by force-directed placement. *Softw.: Pract. Exper.*, 21(11):1129–1164, 1991.